DOI 10.2478/ama-2025-0072

MODELING A TEMPERATURE DISTRIBUTION OF THERMIONIC ENERGY CONVERTER COMPONENTS

Krzysztof SKIBA*, Dariusz KUŚ*, Jarosław SIKORA*

*Faculty of Electrical Engineering and Computer Science, Department of Automation and Metrology
Lublin University of Technology, Nadbystrzycka 38 A, 20-618 Lublin, Poland

k.skiba@pollub.pl, d.kus@pollub.pl, jaroslaw.sikora@pollub.pl

received 12 August 2025, revised 03 November 2025, accepted 03 November 2025

Abstract: Thermionic energy converters, based on the phenomenon of electron thermionic emission, directly convert thermal energy into electrical energy. They are characterized, among other things, by high output power density and potential for integration with high-temperature heat sources. This paper presents a model of a vacuum thermionic energy converter for numerical studies and presents temperature distributions of key components of the converter, including the dispenser cathode, mounting base and ceramic cathode pad, manipulator core, anode, mounting base and ceramic anode pad. The tests were performed in the Ansys 2024 environment in the dispenser cathode temperature range up to 1473,2 K for three electrode mounting base designs made of steel (316L), molybdenum, and copper, respectively. Based on the results obtained, the permissible operating temperature of the cathode mounted on a steel base was determined, at which the emission of toxic vapors from the steel is negligible. The anode temperature values for the three anode mounting base materials and the theoretical limit of energy conversion efficiency were determined. The work emphasizes the need to optimize the selection of materials and mechanical design to improve the durability and efficiency of thermionic energy converters.

Key words: thermionic energy converter, temperature distribution, heat transfer, numerical model

1. INTRODUCTION

Thermionic energy converters (TECs) directly convert thermal energy into electrical energy based on the phenomenon of electron thermionic emission. They are characterized by high output power density, compact design, compatibility with high-temperature heat sources, and theoretically high energy efficiency. These advantages stimulate research into their commercialization. However, the key challenge is to improve the energy efficiency of practical implementations of converters. Research conducted in many renowned scientific centers is focused on obtaining materials for cathodes and anodes with relatively low electron work function and high apparent Richardson constant for the cathode material [1, 2]. Another challenge is to mitigate the negative space charge in the inter-electrode area and to reduce the negative impact of electron reflection from the electrodes [3, 4]. In terms of the mechanical design of the converter, an important issue is to obtain high-temperature and mechanically stable insulators separating the converter electrodes [5]. In order to improve the energy efficiency of converters [6], a number of studies focus on the use of photovoltaic and thermoradiative phenomena in the design of hybrid converters [5, 7, 8, 9].

Dispenser cathodes are efficient sources of electrons that are used in experimental research on thermionic energy conversion. The emission layer of this cathode is sensitive to the influence of metal vapors, including Ag, Au, Ni, Fe (Steels), Pt, Zr [10, 11], whose presence causes an increase in the cathode electron work function and a drastic reduction in the electron thermionic current, an effect known as cathode poisoning. The higher the melting point of the metal, the higher the temperature at which the cathode is poisoned by vapors of that metal. The normalized electron thermionic emission current as a function of temperature and vapor pressure for selected metals is shown in Figs. 1 and 2.

Therefore, it is important to select the right materials for components that come into direct contact with the cathode, in particular the cathode mounting base, the wires connecting the tungsten microheater to the power supply, and the wires connecting the cathode to the load.

The principle of operation of a thermionic energy converter is based on the phenomenon of electron thermionic emission. A schematic diagram of the converter is shown in Fig. 3.

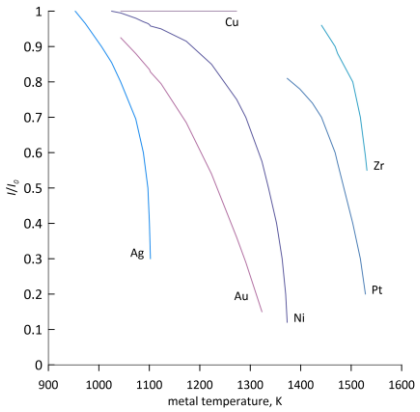

Fig. 1. Normalized electron thermionic emission current of a dispenser cathode operating at 1373.2 K as a function of metal temperature (based on [10, 11])

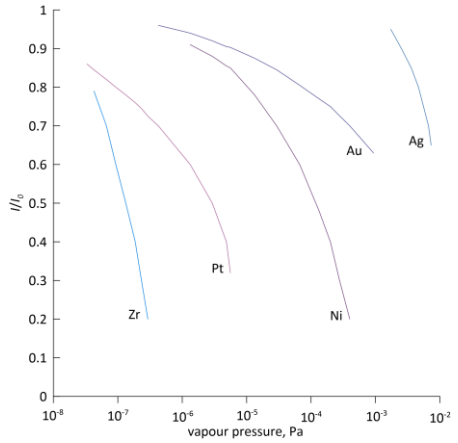

Fig. 2. Normalized electron thermionic emission current of a dispenser cathode operating at 1373.2 K as a function of metal vapor pressure (based on [10, 11])

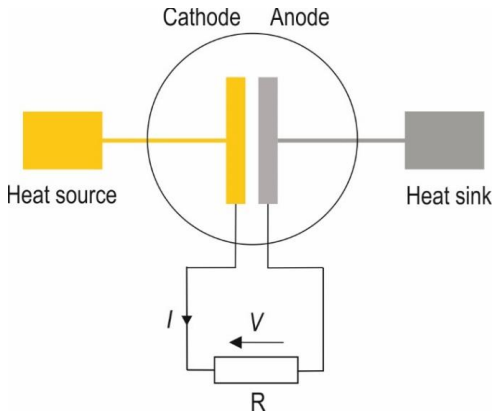

Fig. 3. Schematic diagram of a thermionic energy converter

The electrodes are placed in an ultra-high vacuum chamber and are connected to the load R by means of electrical feedthroughs. The cathode is thermally connected to the heat source, and the anode to the heat receiver. Under the influence of thermal energy supplied to the cathode, electrons are emitted from the cathode surface, then reach the anode by ballistic motion and return to the cathode through the load R. The electrode materials should be selected so that the electron work function ϕ_C of the cathode is greater than the electron work function ϕ_A of the anode.

Fig. 4 shows a schematic distribution of the potential energy of an electron in the cathode-anode region for an ideal converter.

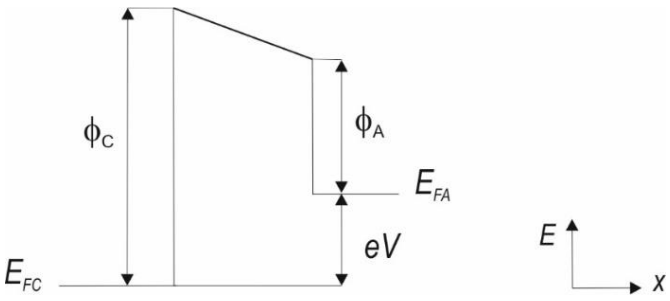

Fig. 4. S. Distribution of potential energy of an electron in the cathode-anode region for an ideal converter (based on [12, 13])

Based on the given potential energy distribution, the load current intensity *I* can be written as follows [12, 13]:

$$I = A_C T_C^2 S_C \, exp\left(-\frac{\phi_C}{kT_C}\right) \quad (1)$$

for: $V \leq \frac{\phi_C - \phi_A}{e}$

$$I = A_A T_A^2 S_A \, exp\left(-\frac{\phi_C - eV}{kT_A}\right) \quad (2)$$

for: $V \geq \frac{\phi_C - \phi_A}{e}$

where $(\phi_C - \phi_A)/e$ is the cathode-anode contact potential, *e* is the elementary charge.

The model *I(V)* dependence in graphical form for an ideal converter is shown in Fig. 5 as a solid line. The calculations were based on the sample data shown on the right side of Fig. 5. For comparison, the *I(V)* characteristic is also shown as a dashed line for a real converter, taking into account the influence of negative space charge, which was determined based on the algorithm [12, 13].

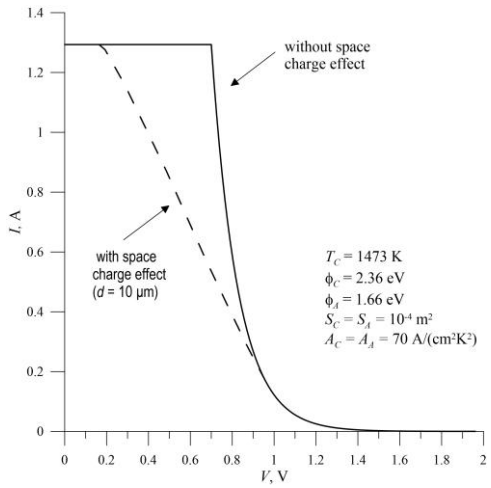

Fig. 5. Model of current-voltage characteristics for an ideal converter and a real converter, taking into account the influence of negative space charge in the cathode-anode area. *d* is the mutual distance between the cathode and the anode

As can be seen in Fig. 5, the load current for the real converter, in the shown output voltage range, is lower than for the ideal converter. In general, for real converters, the load current decreases with increasing cathode-anode distance [14]. Therefore, striving to achieve a small distance between the cathode and anode under conditions of their potentially large temperature difference is a significant technological challenge.

There are many inspiring articles on thermionic energy conversion. However, based on a review of the available literature, it must be noted that there is a lack of studies comparing the effect of electrode base materials on temperature distribution in TECs. Knowledge of the temperature distribution allows the theoretical conversion efficiency limit to be determined, which may justify the selection of appropriate electrode base materials. This paper presents a method for preparing a model for numerical testing and the results of thermal analyses using Ansys 2024 software. The simulation used an energy flow module, a laminar fluid model, a radial temperature propagation model, and a heat exchange model. The tests were carried out for cathode temperatures ranging from 873.2 K to 1473.2 K. Temperature distributions were determined for key converter components in designs using steel, molybdenum, and copper electrode mounting bases, the results were discussed, and the theoretical energy conversion efficiency limit was determined.

DOI 10.2478/ama-2025-0072

2. RESEARCH MODEL

In experimental studies conducted at the Department of Automation and Metrology of the Lublin University of Technology in the field of thermionic conversion of heat into electricity, it is planned to use a dispenser cathode model 311M (HeatWave Labs Inc.) as an electron emitter. A model of the vacuum thermionic energy converter test stand is shown in Fig. 6. The vacuum chamber (Instrument Technology Limited) consists of segments connected by rotary joints, with numerous inter-section contacts and seals, and together with a pump system ensures a vacuum pressure of p=10^{-6} Pa. The interior of the structure is equipped with a precise electrode positioning system, dispenser cathode Model 311M (HeatWave Labs) and a single-axis manipulator Model PMZ-275-2 (Huntington Mechanical Labs, Inc.) for adjusting the width of the interelectrode gap, which allows for precise positioning of the electrodes relative to each other. The cathode, integrated in a molybdenum housing with a tungsten microheater operating in the range of 1173 K–1473.2 K, is characterized by a relatively high electron emission current density of up to 5 A/cm² at 1473.2 K. The chamber has a flange for connection to an ionization vacuum gauge and flanges with vacuum electrical feedthroughs for connecting tungsten microheaters and thermocouples to a temperature controller and data acquisition system.

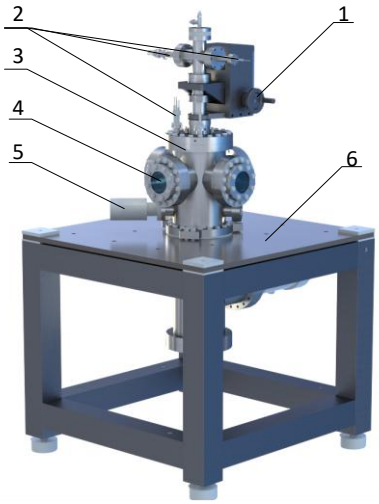

Fig. 6. Model of a vacuum thermionic heat-to-electric energy converter test stand. 1 – manipulator, 2 – vacuum electrical feedthroughs, 3 – vacuum chamber, 4 – viewing window, 5 - vacuum gauge, 6 - test stand frame

The geometric model of the chamber was developed in a CAD environment and then imported into the Ansys Workbench 2024 platform, where the subsequent stages of preparing the model for thermal analysis were carried out. The cylinder of the test chamber has a diameter of 0.16 m, and the geometric volume of the chamber is 0.01 m³. Due to the characteristics of the finite element method and the need to ensure convergence of calculations in the SpaceClaim module, the geometry was simplified. To this end, roundings, chamfers, technological openings, and other details irrelevant to heat conduction were removed. Component assemblies were replaced with homogeneous solids with equivalent thermal properties. Elements made of different materials were defined as separate geometric domains, which made it possible to assign individual thermal conductivity parameters and emissivity coefficients to them. Particular attention was paid to the correct mapping of contact surfaces, eliminating gaps and wall penetration (so-called coincident faces), which could interfere with the analysis of heat conduction and radiation. The geometric model was verified using the Repair Geometry and Detect Gaps tools, removing topological errors and preparing the model for the discratization process. A cross-sectional view of the prepared model is shown in Fig. 7. In the upper part of the structure, the following can be distinguished: the manipulator core (1) made of 316L stainless steel, a ceramic cathode pad (2) made of Al_2O_3 , the cathode mounting base with mounting elements (3), the 311 M cathode dispenser in a molybdenum housing (6), inside which an insulating section (4) and a heating section (5) with a tungsten microheater were separated. The microheater is embedded in a structure filling the interior of the electrode with aluminum oxide. The lower part of the drawing shows the 311M electrode forming the anode, the mounting base (8) of the anode and the ceramic spacer (10). Between the cathode (6) and the anode (7) there is a gap with adjustable width.

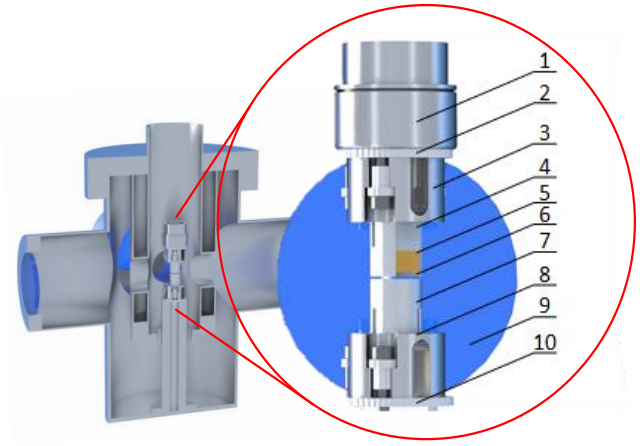

Fig. 7. Virtual model of the chamber in a semi-cross-section view, adapted for numerical analysis. 1 – manipulator core, 2 – ceramic cathode pad, 3 – cathode mounting base, 4 – internal cathode insulation (half-cross-section view), 5 – cathode heater, 6 – cathode front surface, 7 – anode, 8 – anode mounting base, 9 – borosilicate glass of the viewfinder,10 – ceramic anode pad

The model was discretized in the Ansys Meshing module. Tetrahedral elements were used, with a particularly dense mesh in areas where large temperature gradients were expected, especially near the heater and at the boundaries of material contacts. A hybrid approach was adopted, in which the global element size was set to 5 mm, while locally Face Sizing and Body Sizing functions were used with a maximum element size of 0.2 mm. In these areas, five inflation layers were added with a gradual increase in mesh density, in accordance with the recommendations for mesh sensitivity under vacuum conditions [15]. The total number of elements was approximately 1.25 million, which allowed a compromise to be reached between the accuracy of the geometry representation and the calculation time (Fig. 8). The generated mesh was evaluated in terms of element quality. The minimum element quality value was 0.08, and the maximum skewness reached 0.95, which falls within the acceptable range for steady-state thermal analyses. The average skewness value for all elements was 0.28, indicating good mesh uniformity. The skewness distribution histogram shows that more than 75 % of the elements have skewness values below 0.5.

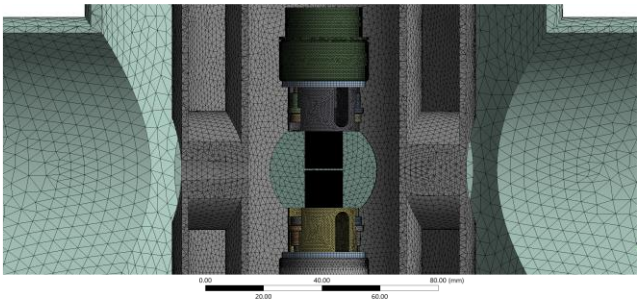

Fig. 8. Discrete model of the test chamber

The interior of the high-vacuum chamber was modeled as a space filled with as a vacuum region with zero density and thermal conductivity, which means that there is no convection. The inner walls of the chamber, electrodes, electrode bases, insulators, and other components were defined as surfaces participating in radiation exchange. The model uses the Surface to Surface Radiation (S2S) method [16], which allows for the consideration of thermal radiation between ("visible") surfaces without the involvement of an intermediate medium. The S2S model assumes that radiation occurs between gray bodies and does not take into account scattering or absorption by the medium, which makes it ideal for vacuum conditions [17]. Energy exchange is described by an equation, in accordance with the literature [18, 19]:

$$q_i = \varepsilon_i \sigma \left(T_i^4 - \sum_{j=1}^{N} F_{ij} T_j^4 \right) \tag{3}$$

where: q_i – heat energy flux radiated from surface i, ε_i – emissivity coefficient of surface i, σ – Stefan-Boltzmann constant, T_i , T_j – surface temperatures i, j, F_{ij} – visibility coefficient between surfaces i and j, N – number of all surfaces participating in energy exchange by radiation.

For external walls, the phenomenon of free convection with the surrounding air was taken into account. A convection boundary condition was applied, assuming an ambient temperature of 298.0 K and atmospheric pressure of 101325 Pa. A convection coefficient of 5 W/(m²K) was adopted, in accordance with the literature [23], which allows for a realistic estimation of heat losses to the environment. In addition, the chamber is equipped with a liquid cooling system for the manipulator core, which limits the change in the gap width due to thermal expansion of the manipulator components. The thermal properties of the materials used were taken from specialist literature [20-25]. The thermal conductivity, specific heat, density, and emissivity of the individual materials are summarized in Tab. 1. Energy fluxes associated with electron transport between the cathode and anode, as well as the effects of temperature-dependent material properties, were not included in this model. Extending the model will be considered in future work.

Tab. 1. Thermal and physical properties of materials used in the model

Material	Thermal Conductivity [W/(m·K)]	Specific heat [J/(kg·K)]	Density [kg/m³]	Emissivity [–]
Stainless Steel 316L	16.2	500.0	8000	0.28
Molybdenum (Mo)	138.0	250.0	10200	0.05
Copper (Cu)	398.0	385.0	8960	0.03
Aluminum Oxide (Al_2O_3)	30.0	880.0	3960	0.25
Pyrex 7740 borosilicate glass	1.14	830.0	2230	0.92

The simulations were carried out for cathode temperatures in the range 873.2 K - 1473.2 K. A relatively low initial temperature was chosen in order to illustrate trends in temperature distributions. The maximum operating temperature of the 311M dispenser cathode is 1473.2 K. This temperature was adopted as the boundary condition in the model tests. The heat source was defined by setting the temperature of the tungsten microheater of the cathode.

3. RESULTS OF NUMERICAL ANALYSES

The temperature distribution in the vacuum chamber of the converter, in which the temperature of the tungsten microheater of the cathode is 1473.2 K and the electrode bases are made of stainless steel, is shown in Fig. 9.

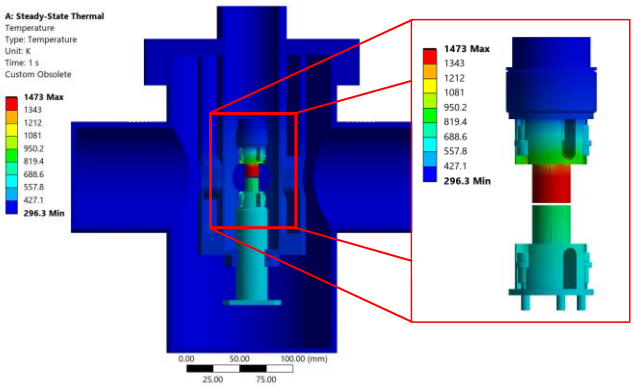

Fig. 9. Temperature distribution in the test chamber model

The detailed temperature distribution of the cathode is illustrated in Fig. 10. The minimum temperature, recorded at the mounting base, is significantly lower and reaches 780.4 K, which indicates a strong temperature gradient along the electrode.

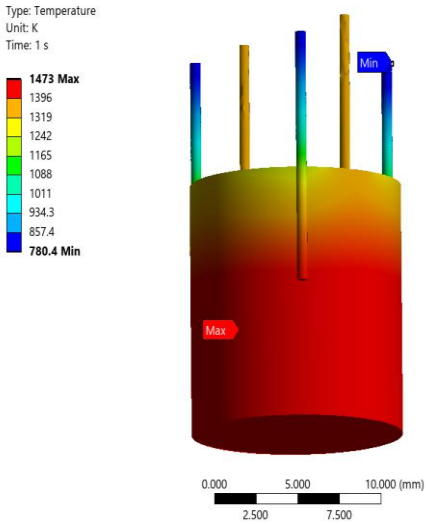

Fig. 10. Temperature distribution in the cathode model

The temperature distribution of the anode, shown in Fig. 11, shows its heating in the front part to a temperature of 817.8 K. The temperature along the electrode decreases towards the mounting base, reaching a minimum value of 662.2 K.

DOI 10.2478/ama-2025-0072

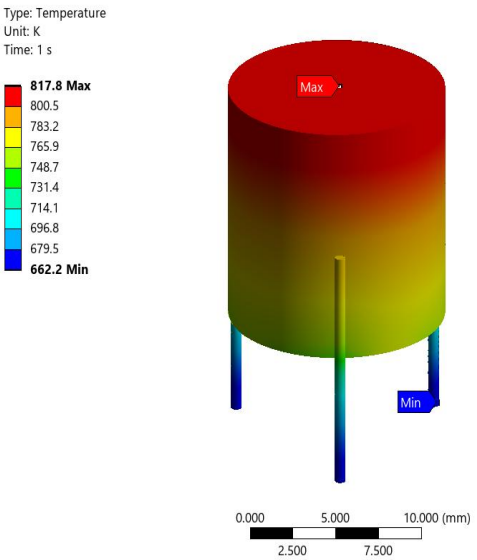

Fig. 11. Temperature distribution in the anode model

Fig. 12 shows the temperature distribution in the cathode mounting base. The area where the steel base makes contact with the cathode is noteworthy. In this region, the base temperature reaches 1359.1 K, causing steel vapor to contaminate the cathode emission surface. Due to the constituents of 316L stainless steel, particularly its relatively high nickel content, contamination of the cathode surface decreases the thermionic emission current.

As can be seen from the nickel curves in Fig. 1 and Fig. 2, the normalized thermionic emission current will significantly decrease at a base temperature of 1359.1 K and a pressure below $1.3 \cdot 10^{-5}$ Pa.

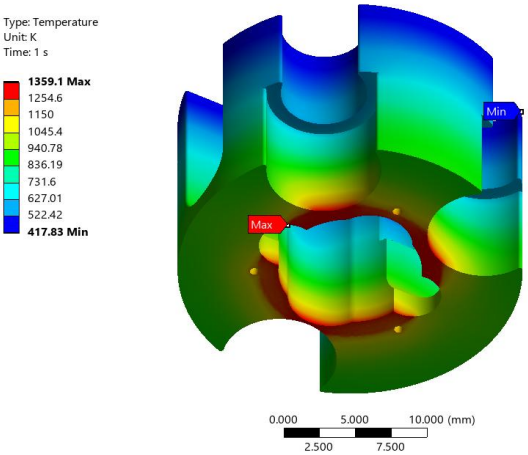

Fig. 12. Temperature distribution in the cathode mounting base model

On the anode side, as can be seen in Fig. 13, the temperature of the mounting base in the area of direct contact with the anode reaches 764.8 K and the evaporation effect of the steel base is negligible.

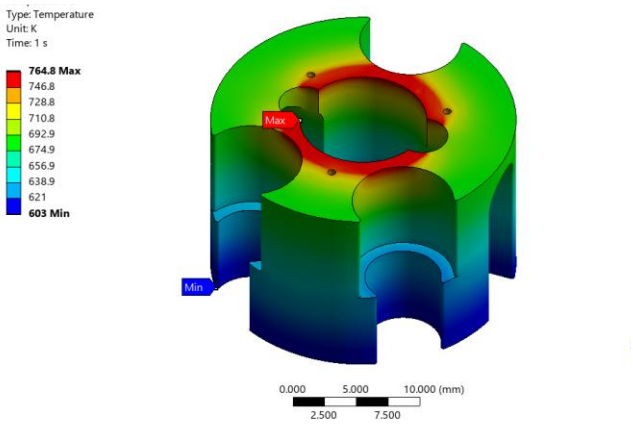

Fig. 13. Temperature distribution in the anode mounting base model

The temperature distribution for the ceramic cathode pad made of aluminum oxide (markings 2 and 10 in Fig. 7) is shown in Fig. 14. The maximum temperature of the pad is 446.6 K.

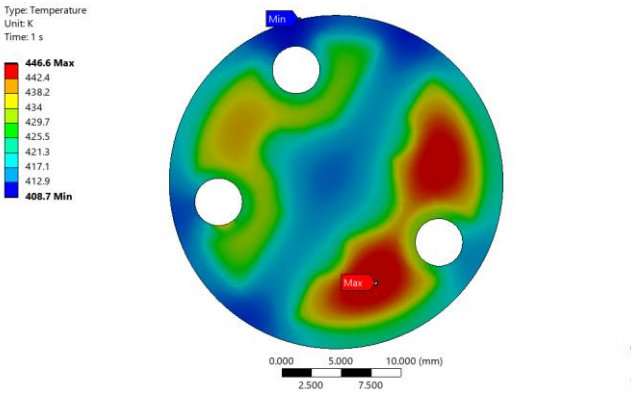

Fig. 14. Temperature distribution in the model of the cathode ceramic pad surface

The manipulator core, which remains in contact with the ceramic pad, reaches a temperature of 425.5 K, as illustrated in Fig. 15.

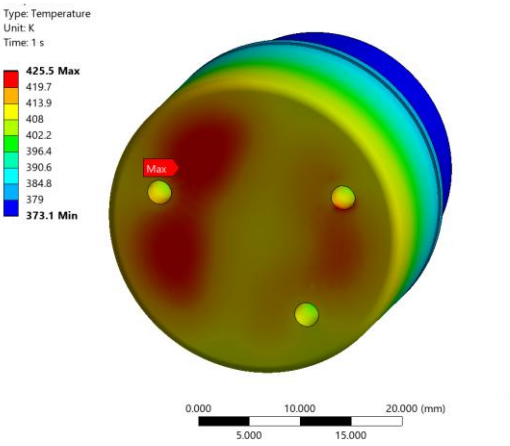

Fig. 15. Temperature distribution in the manipulator core model

On the anode side, according to Fig. 16, the temperature of the ceramic pad is 608.6 K. The lower temperature of the cathode pad and the manipulator core compared to the anode temperature is due to the liquid cooling of the manipulator core.

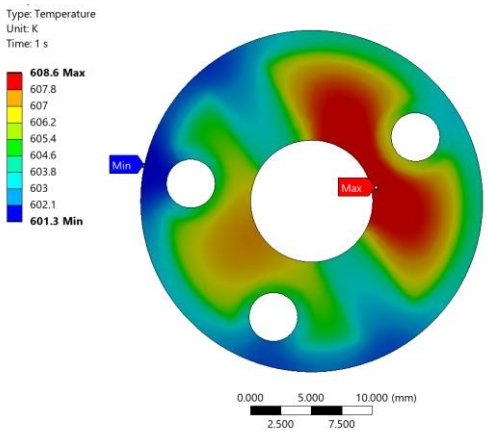

Fig. 16. Temperature distribution in the model of the anode ceramic pad surface

In the analyzed system, a significant temperature gradient was observed along the vertical axis of the cathode base at a height of 15 mm. For the element made of steel, the temperature decreases from a maximum value of 1359.1 K to a minimum of 417.8 K, corresponding to a difference of ΔT = 941.3 K. The temperature variation propagates from the inner edge toward the outer surface. Potential areas of thermal stress concentration are located on the wall in the immediate vicinity of the cathode. For the base made of molybdenum, the temperature decreases from 978.6 K to 543.1 K (ΔT = 435.5 K), while for copper, the corresponding values are 806.2 K and 596.7 K (ΔT = 209.5 K). Compared to the steel base, the temperature gradient is reduced by approximately 53.7% for molybdenum and 77.7% for copper. The obtained results clearly indicate that an increase in the thermal conductivity of the material leads to a distinct reduction in the temperature gradient within the analyzed region. Consequently, the use of materials with high thermal conductivity, such as molybdenum and copper, promotes a more uniform temperature distribution and limits the formation of thermal stresses within the structural components of the electrode assembly.

To avoid potential contamination of the cathode emission surface by 316L stainless steel component vapors, particularly toxic nickel vapor, under high temperature conditions (Fig. 12), the temperature limit for the steel cathode base was determined based on the arbitrary criterion of a 5% permissible decrease in electron emission current. Based on the curve for nickel shown in Figure 1, the temperature at which the electron emission current drops by 5% was estimated to be 1133.2 K. In order to determine the maximum cathode temperature under these conditions, the temperatures of the cathode, cathode base, anode, and anode base were determined as a function of the tungsten microheater temperature in the range from 873.2 K to 1473.2 K, which are presented in Tab. 2.

Tab. 2. Temperature values of key converter components as a function of tungsten microheater temperature in a design with bases made of 316L steel

T_{heater} [K]		873.2	973.2	1073.2	1173.2	1273.2	1373.2	1473.2
Cathode	$T_{average}$	839.7	932.8	1025.8	1118.7	1211.4	1304.0	1396.4
	T_{max}	873.2	973.2	1073.2	1173.2	1273.2	1373.2	1473.2
	T_{min}	555.7	592.1	628.4	664.6	700.7	736.6	780.4
Cathode base	$T_{average}$	540.1	573.4	606.6	639.6	672.6	705.5	738.2
	T_{max}	817.3	905.7	993.8	1081.5	1169.0	1255.9	1359.1
	T_{min}	393.4	397.5	401.6	405.8	409.9	414.0	417.8
Anode	$T_{average}$	420.3	465.9	517.9	576.2	640.0	709.3	783.6
	T_{max}	424.8	472.8	528.0	590.4	659.4	735.1	817.8
	T_{min}	403.4	440.1	480.1	523.0	567.9	614.5	662.2
Anode base	$T_{average}$	402.2	438.2	477.4	519.3	562.9	607.9	653.8
	T_{max}	417.9	462.2	512.5	568.5	629.5	695.3	764.8
	T_{min}	394.8	426.9	461.0	496.5	532.2	567.9	603.2

The above data show that in order to limit the cathode base temperature to 1133.2 K, the permissible microheater temperature should not exceed 1223.2 K. This limit is presented only as a safety constraint and not as a practical operating point since emission current densities are relatively low at such temperatures. Under these conditions, the anode temperature is approximately 623,2 K. The specified cathode and anode temperatures allow the energy conversion efficiency to be estimated. Converter efficiency is defined as the ratio of output power density to total input heat flux to the cathode [1] and it takes into account all real heat loss mechanisms, including those resulting from radiation from the cathode to the anode, thermal conductivity through the cathode base material and lead wires, backward emission of electrons from the anode to the cathode. In our research, in order to compare the impact of electrode base materials on the temperature distribution of converter components and, consequently, on conversion efficiency, we used the theoretical conversion efficiency limit determined based on the Carnot engine formula [1]:

$$\eta_{Carnot} = \left(1 - \frac{T_{cold}}{T_{hot}}\right) \cdot 100\% \tag{4}$$

where: T_{cold} and T_{hot} are hot and cold reservoir temperatures, respectively.

For a design with 316L steel electrode bases, the maximum theoretical energy conversion efficiency is approximately 49% at a tungsten microheater temperature of 1223.2 K.

Limiting the temperature of the tungsten microheater to 1223.2 K ensures suitable operating conditions for the cathode, eliminating the effect of steel vapors poisoning the emitting surface. However, in this case, the full operating temperature range of the cathode, i.e up to 1473.2 K, is not utilized. As a result, the range of electron thermionic emission current, which is the output current of the converter, is also limited. In order to achieve a cathode temperature of 1473.2 K, the electrode bases should be made of materials whose vapors do not poison the cathode emission surface at a given temperature, such as molybdenum or copper [10, 11]. Using the developed research tool, temperature distributions were determined for key converter components in designs with molybdenum and copper bases, respectively. Table 3 shows the results for the converter design with molybdenum bases.

DOI 10.2478/ama-2025-0072

Tab. 3. Temperature values of key converter components as a function of tungsten microheater temperature for design with molybdenum bases

T_{heater} [K]		873.2	973.2	1073.2	1173.2	1273.2	1373.2	1473.2
Cathode	$T_{average}$	795.5	879.9	964.2	1048.6	1132.8	1217.0	1300.7
	T_{max}	873.2	973.2	1073.2	1173.2	1273.2	1373.2	1473.2
	T_{min}	520.9	550.4	579.9	609.3	638.7	668.0	697.2
Cathode base	$T_{average}$	516.4	544.9	573.5	602.0	630.5	658.9	687.2
	T_{max}	649.4	704.5	759.6	814.5	869.4	924.2	978.6
	T_{min}	450.6	466.1	481.5	497.0	512.4	527.8	543.1
Anode	$T_{average}$	397.9	432.1	468.8	507.7	548.6	590.8	633.6
	T_{max}	408.0	447.6	491.8	540.5	593.7	651.4	713.1
	T_{min}	404.0	441.5	482.7	527.6	575.9	627.5	681.6
Anode base	$T_{average}$	397.8	432.0	468.6	507.4	548.2	590.3	632.9
	T_{max}	400.1	435.5	473.8	514.9	558.5	604.0	650.9
	T_{min}	396.7	430.3	466.1	503.8	543.3	583.7	624.3

In this design solution, the maximum temperature of the microheater can be 1473.2 K and then, as can be seen in the above summary of results, the maximum temperature of the anode is 713.1 K. The theoretical limit of heat-to-electric energy conversion efficiency, based on the Carnot engine equation, is 51.6%. It is worth noting the comparison of the base temperatures of steel and molybdenum. Assuming a hypothetical microheater temperature of 1473.2 K in both designs, the maximum temperature of the steel cathode base would be 1359.1 K (Tab. 2), and that of the molybdenum base would be 978.6 K (Tab. 3). The significant difference in temperature values results from the relatively high thermal conductivity of molybdenum (Tab. 1).

Table 4 presents the results for the converter design with copper bases.

Tab. 4. Temperature values of key converter components as a function of tungsten microheater temperature for design with copper bases

T_{heater} [K]		873.2	973.2	1073.2	1173.2	1273.2	1373.2	1473.2
Cathode	$T_{average}$	779.4	860.6	941.8	1022.9	1104.0	1185.0	1266.0
	T_{max}	873.2	973.2	1073.2	1173.2	1273.2	1373.2	1473.2
	T_{min}	509.1	536.3	563.5	590.6	617.7	644.7	671.7
Cathode base	$T_{average}$	509.1	536.2	563.3	590.4	617.5	644.5	671.5
	T_{max}	570.4	609.8	649.2	688.5	727.8	767.0	806.2
	T_{min}	474.9	495.3	515.6	535.9	556.2	576.4	596.7
Anode	$T_{average}$	402.3	438.9	479.0	522.3	568.7	618.0	669.7
	T_{max}	406.3	445.1	488.0	535.2	586.6	642.0	701.4
	T_{min}	397.4	431.3	467.7	506.2	546.5	588.2	630.5
Anode base	$T_{average}$	397.4	431.3	467.6	506.1	546.5	588.1	630.4
	T_{max}	398.2	432.5	469.5	508.8	550.1	593.0	636.9
	T_{min}	396.9	430.6	466.6	504.7	544.4	585.3	626.9

For a microheater temperature of 1473.2 K, the maximum temperature of the copper cathode base is 806.2 K. The maximum anode temperature is 701.4 K. The theoretical limit of thermal energy conversion efficiency, determined based on the Carnot engine relationship, is 52.4%. In this case, the higher energy efficiency compared to the efficiency for design with molybdenum bases results from the nearly three times higher thermal conductivity of copper compared to molybdenum (Tab. 1), and consequently lower anode temperature.

For practical TEC operation, our results for the temperature differences between the cathode and anode are approximately 613.7 K–653.3 K for stainless steel 316L, 679.4–760.0 K for molybdenum and 686.6 K–771.7 K for copper. These are in agreement with the experimental ranges reported for thermionic energy converters [1, 26–29], where the typical cathode temperatures within the effective operating range are 1273.2 K–1473.2 K and the anode temperatures are 573.2 K–773.2 K. The agreement between the modelled and measured temperature gradients confirms the usefulness of the developed numerical model.

To compare the test results for the three cathode base materials, Fig. 17 illustrates the relationship between maximum cathode base temperature and heater temperature.

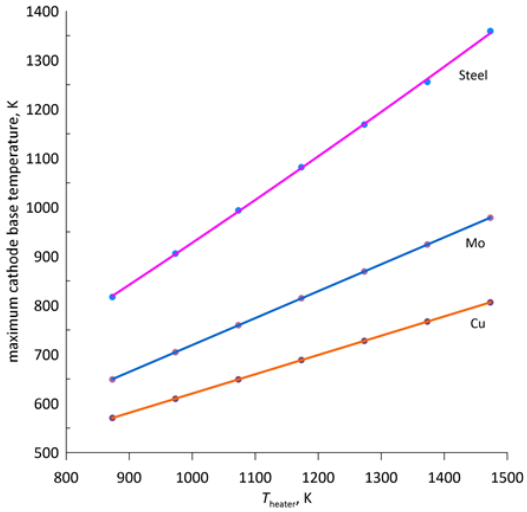

Fig. 17. A comparative graph of the maximum cathode base temperature for three materials as a function of heater temperature

For a complete comparison, the upper range of the heater temperature was assumed to be the same for all three materials. The significant temperature differences observed in the tested materials are the result of varying heat dissipation. Mounting the cathode on a base causes heat loss because a significant amount of heat is transferred from the microheater through the base and into the vacuum chamber support. From a heat balance and energy efficiency standpoint, this is an unfavorable design. In this context, and considering the sensitivity of the dispenser cathode to contamination, molybdenum is the preferred material for its base.

Figure 18 shows the maximum anode temperature in relation to the heater temperature for three base anode materials.

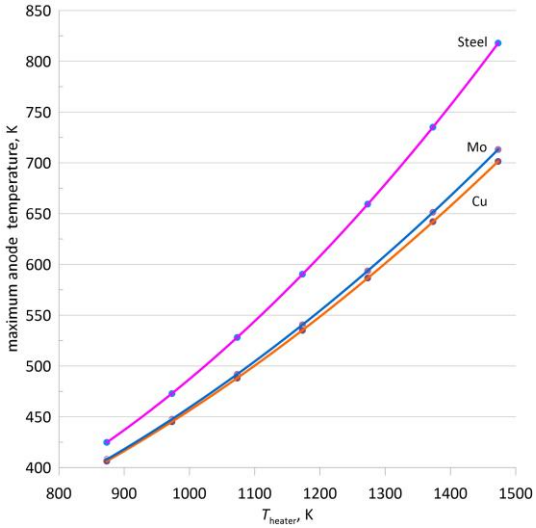

Fig. 18. A comparative graph of the maximum anode temperature for three materials as a function of cathode temperature

The temperature differences between the anodes are also caused to a significant extent by the heat dissipation from the anode through the anode base to the vacuum chamber supports. The anode mounted on a copper base reaches the lowest temperature, while the anode mounted on a molybdenum base reaches a slightly higher temperature. From the perspective of the theoretical energy efficiency limit (formula (4)), a low anode temperature is advantageous, so it can be assumed that copper is the preferred material for the anode base.

In practical prototype designs of thermionic energy converters, the distance between the cathode and anode is usually less than 100 μm, so the thermal expansion coefficient of the material should also be taken into account when selecting the electrode base material. In this context, the preferred material is molybdenum, which has low thermal expansion, high strength at elevated temperatures and reduced thermal deformation.

4. CONCLUSIONS

Thermionic energy converters are essential for working with high-temperature energy sources, as well as for potential applications in hybrid energy technologies and space systems. This article presented the development and numerical analysis of a vacuum thermionic energy converter model using the ANSYS 2024 simulation environment. The study focused on the temperature distribution within key internal components — namely the cathode, anode, mounting bases, ceramic insulating pads, and the manipulator core for various electrode base materials, including stainless steel (316L), molybdenum, and copper, across a cathode heater temperature range of up to 1473.2 K. The obtained results confirmed that the choice of electrode mounting base material significantly affects the thermal characteristics of the system. Stainless steel, despite its favorable mechanical properties and ease of processing, causes a substantial temperature increase in the cathode base, which can lead to the release of metal vapors and degradation of the emitter surface. This phenomenon, known as cathode poisoning, directly reduces emission efficiency and long-term operational stability. Based on the analysis, a safe operating limit was established for the steel mounting base. The results indicate that the microheater temperature should not exceed 1223.2 K to prevent excessive heating of the cathode base and ensure stable emission parameters. In contrast, molybdenum and copper bases demonstrated significantly better thermal behavior. Due to their higher thermal conductivity, both materials effectively reduce the temperature in the cathode base region, enabling safe operation at elevated cathode temperatures. The maximum theoretical energy conversion efficiency, calculated based on Carnot cycle assumptions, was achieved for the copper-based design (52.4%), attributed to the significantly lower anode temperature. Based on the results, molybdenum should be assumed to be the preferred material for the cathode base and copper for the anode base. Future research will involve optimization of component geometry to minimize thermal resistance, experimental validation of numerical results, and evaluation of alternative structural materials suitable for operation in high-temperature vacuum environments. Additionally, the mechanical behavior of mounting materials under cyclic thermal loading should be investigated. The findings emphasize that material selection and thermal design play a decisive role in determining the operational efficiency, durability, and applicability of thermionic energy converters in high-temperature energy systems. The results provide a foundation for further optimization aimed at improving thermal stability and energy conversion efficiency in next-generation thermionic devices.

REFERENCES

1. Campbell MF, Celenza TJ, Schmitt F, Schwede JW, Bargatin I. Progress Toward High Power Output in Thermionic Energy Converters. Advanced Science. 2021; 8: 2003812. https://doi.org/10.1002/advs.202003812
2. Hao M, Xiao G, Qiu H. Experimental characteristics of thermionic energy converters employing barium-dispenser cathode and semiconductor anodes. Energy. 2025; 325: 136132. https://doi.org/10.1016/j.energy.2025.136132
3. Wanke R, Voesch W, Rastegar I, Kyriazis A, Braun W, Mannhart J. Thermoelectronic energy conversion: Concepts and materials. MRS Bulletin. 2017; 42: 518-524. https://doi.org/10.1557/mrs.2017.140
4. Lim IT, Lambert SA, Vay JL, Schwede JW. Electron reflection in thermionic energy converters. Applied Physics Letters. 2018;112: 073906. https://doi.org/10.1063/1.5018067
5. Bellucci A, Girolami M, Trucchi DM. Chapter 10 - thermionic and thermoelectric energy conversion, in: Datas A (Ed.) Ultra-High Temperature Thermal Energy Storage. Transfer and Conversion. Woodhead Publishing. 2021;253–284. Woodhead Publishing Series in Energy. https://doi.org/10.1016/B978-0-12-819955-8.00010-7
6. Hu C, Liang T, Chen X, Su S, Chen J. Graphene-anode thermionic converter demonstrating total photon reflection. Applied Physics Letters 2021; 118: 083901. https://doi.org/10.1063/5.0039113
7. Bellucci A, García-Linares P, Martí A, Daniele Maria Trucchi DM, Datas A. A Three-Terminal Hybrid Thermionic-Photovoltaic Energy Converter. Applied Physics Letters. 2021; 118: 083901. https://doi.org/10.1002/aenm.202200357
8. Qiu H, Lin S, Haoran Xu H, Hao G, Xiao G. Experimental and theoretical study on hybrid thermionic-photovoltaic energy converters with graphene/semiconductor Schottky junction. Energy Conversion and Management. 2023; 276: 116584. https://doi.org/10.1016/j.enconman.2022.116584
9. Zhang X, Ye Z, Su S, Chen J. Thermionic-Thermoradiative Converters. IEEE Electron Device Letters. 2018; 39 (9): 1429-1432. https://doi.org/10.1109/LED.2018.2859797
10. Practical Aspects of Modern Dispenser Cathodes, tb-134, https://www.cathode.com/pdf/tb-134.pdf
11. Vaughn J, Dudley K, Lesensky L. The deactivation of impregnated type cathodes due to metal vapors. Vacuum. 1961; 11: 77-79. https://doi.org/10.1016/0042-207X(61)90011-2
12. Hatsopoulos G N, Gyftopoulos E P. Thermionic Energy Conversion. Cambridge MA: MIT Press. 1973; 1.
13. Sikora J. Thermionic electron emission sources: biasing conditions. Lublin: Lublin University of Technology Publishing House; 2019. [in Polish]. https://hdl.handle.net/20.500.14629/487
14. Lee J-H, Bargatin I, Melosh N A, Howe R T. Optimal emitter-collector gap for thermionic energy converters. Applied Physics Letters. 2012; 100: 173904.https://doi.org/10.1063/1.4707379
15. Badshah S, Atif M, Ul Haq I, Abdullah Malik S, Badshah M, Jan S. Thermal Analysis of Vacuum Resistance Furnace. Processes. 2019;7:907.https://doi.org/10.3390/pr7120907
16. Howell JR, Mengüç MP, Siegel R. Thermal Radiation Heat Transfer. 7th ed. Boca Raton: CRC Press; 2021. https://doi.org/10.1201/9781439894552
17. ANSYS Inc. ANSYS Fluent Tutorial Guide. Chapter: Radiation Heat Transfer Models. Canonsburg (PA): ANSYS Inc.; 2023.
18. Büschgens D, Schubert C, Pfeifer H, Radiation modelling of arbitrary two-dimensional surfaces using the surface-to-surface approach extended with a blocking algorithm. Heat and Mass Transfer. 2021; 57:1577–1590. https://doi.org/10.1007/s00231-022-03203-4
19. Incropera FP, DeWitt DP, Bergman TL, Lavine AS. Fundamentals of Heat and Mass Transfer. 8th ed. Hoboken: Wiley; 2017. ISBN: 978-1-

DOI 10.2478/ama-2025-0072

119-32042-5.
20. Mekky AB. Computational modelling for specific heat and thermal conductivity of austenitic stainless steels alloys at solid phase. Revue des Composites et des Matériaux Avancés. 2020;30(1):25–33. https://doi.org/10.18280/rcma.300104
21. ASM International. ASM Ready Reference: Thermal Properties of Metals and Alloys. ASM International. Materials Park. OH. USA. 2002. ISBN: 978-0-87170-768-0.
22. Terada Y, Ohkubo K, Mohri T, Suzuki T. Thermal Conductivity of Intermetallic Compounds with Metallic Bonding. Materials Transactions. 2002; 43 (12): 3167–3176.https://doi.org/10.2320/matertrans.43.3167
23. Zhang A, Li Y. Thermal Conductivity of Aluminum Alloys - A Review. Materials. 2023;16(8): 2972. https://doi.org/10.3390/ma16082972
24. Goodfellow Cambridge Ltd., Molybdenum Sputtering Target – Product No. MO00-ST-000200 (Mo 99.9 %) – Technical Data Sheet. Goodfellow Cambridge Ltd. Maldon UK. 2025. https://www.goodfellow.com/global/molybdenum-sputtering-target-group
25. Frolec J, Králík T. An overview of the thermal radiative properties of metallic materials. Proceedings of the 15th IIR International Conference Cryogenics. Prague Czech Rep. 2019;8-11. https://doi.org/10.18462/iir.cryo.2019.0028
26. Baragiola RA, Ferron J, Vidal F. Operation and oxidation of thermionic dispenser cathodes studied by high-resolution photoemission. Journal of Vacuum Science & Technology A. 1998; 16(5); 2309–2316. https://doi.org/10.1116/1.581345
27. Forman R et al. Surface studies of thermionic cathodes and the mechanism of operation. NASA Technical Report. NASA TM X-73532; 1976.https://ntrs.nasa.gov/api/citations/19760024327/downloads/19760024327.pdf
28. Huffman FN et al. High efficiency thermionic converter studies. NASA Technical Report. NASA CR-135183; 1977. https://ntrs.nasa.gov/api/citations/19770006877/downloads/19770006877.pdf
29. Gao JY, Yang Y, Zhang XK, Li SL, Hu P, Wang JS. A review on recent progress of thermionic cathode. 2020;182: 109735. https://doi.org/10.1007/s42864-020-00059-1

Krzysztof Skiba: https://orcid.org/0000-0001-5504-3946

Dariusz Kuś : https://orcid.org/0000-0002-8010-8307

Jarosław Sikora: https://orcid.org/0000-0003-4843-0731